Research Article Vol. 59, No. 2 / 10 January 2020 / Applied Optics 271

applied optics

Characterization of optofluidic devices for the sorting of sub-micrometer particles

James White,[1,4] Cyril Laplane,[2,4] Reece P. Roberts,[2,4] Louise J. Brown,[3,5] Thomas Volz,[2,4] and David W. Inglis[1,5,*]

[1]School of Engineering, Macquarie University, Macquarie Park, NSW 2109, Australia
[2]Department of Physics and Astronomy, Macquarie University, Macquarie Park, NSW 2109, Australia
[3]Department of Molecular Sciences, Macquarie University, Macquarie Park, NSW 2109, Australia
[4]ARC Centre of Excellence for Engineered Quantum Systems, Macquarie University, Macquarie Park, NSW 2109, Australia
[5]ARC Centre of Excellence for Nanoscale BioPhotonics, Macquarie University, Macquarie Park, NSW 2109, Australia
*Corresponding author: david.inglis@mq.edu.au

Received 30 September 2019; revised 18 November 2019; accepted 21 November 2019; posted 22 November 2019 (Doc. ID 379109); published 6 January 2020

In this work, we investigate methods of fabricating a device for the optical actuation of nanoparticles. To create the microfluidic channel, we pursued three fabrication methods: SU-8 to molded polydimethylsiloxane soft lithography, laser etching of glass, and deep reactive ion etching of fused silica. We measured the surface roughness of the etched sidewalls, and the laser power transmission through each device. We then measured the radiation pressure on 0.5-μm particles in the best-performing fabricated device (etched fused silica) and in a square glass capillary. © 2020 Optical Society of America

https://doi.org/10.1364/AO.59.000271

1. INTRODUCTION

The radiation pressure of laser light has been used to affect the motion of particles for 50 years since the pioneering work of Ashkin [1]. A recent review of optical particle manipulation is provided by Bradshaw and Andrews [2]. There are two types of optical forces: the gradient force, typically used to confine particles in optical tweezers, and the radiation pressure force, which acts in the direction of beam propagation. Radiation pressure is commonly used for particle sorting in a fluidic channel.

Sorting can be active, where some particle property is interrogated, then a sorting action is taken [3,4]. Or it can be passive, where the actuation is always engaged but acts differently on different particles [5–7]. In passive applications, the actuating laser beam is usually orthogonal to the viewing axis and may be brought to the fluid channel through waveguides [3,4,6], collimation, or focusing [5,7].

Optical radiation forces depend on the transmitted momentum of the optical beam inside the sorting channel. This is significantly affected by the fluidic chamber's sidewall, through which the field must be transmitted. A sidewall that is rough in comparison to the wavelength will show diffuse reflection, and the beam will lose much of its forward momentum. A sidewall whose roughness is much smaller than the wavelength will transmit the beam with very little scattering [8].

The sidewall surface roughness is produced by the method of fabrication, and there are many ways to fabricate optofluidic devices. Laser machining can be well suited, particularly because of its ability to produce truly 3D structures, including curved walls for lensing [9]. However, this process usually involves a second step of etching with hydrofluoric acid to clear modified glass and/or to smooth surfaces. 3D printing can also produce 3D parts with optical surfaces [10]; however, there is a trade-off between part size and surface roughness that limits current use. Hawkins and Schmidt reviewed fabrication methods for creating fluid-filled waveguide structures. These include anisotropic wet and deep reactive ion etched (DRIE) etching of silicon wafers followed by metallic, chemical vapor deposition (CVD) dielectric or polymer coatings, and the use of sacrificial materials to form channels [11].

In this work, we investigate the effect of various fabrication approaches (without post-fabrication wet etching) for a general purpose optofluidic sorting device [Fig. 1(a)]. We compare the power transmitted through the fluid channel for all fabrication methods. Finally, we compare the radiation pressure on sub-micrometer particles in our best device against commercially available rectangular glass capillaries. To the best of our knowledge, this is the first time that effect of fabrication method on radiation pressure has been studied.

2. FABRICATION

Devices were designed as a 2D layout to be fabricated to a desired depth [Fig. 1(b)]. Each device has two inlet ports, two

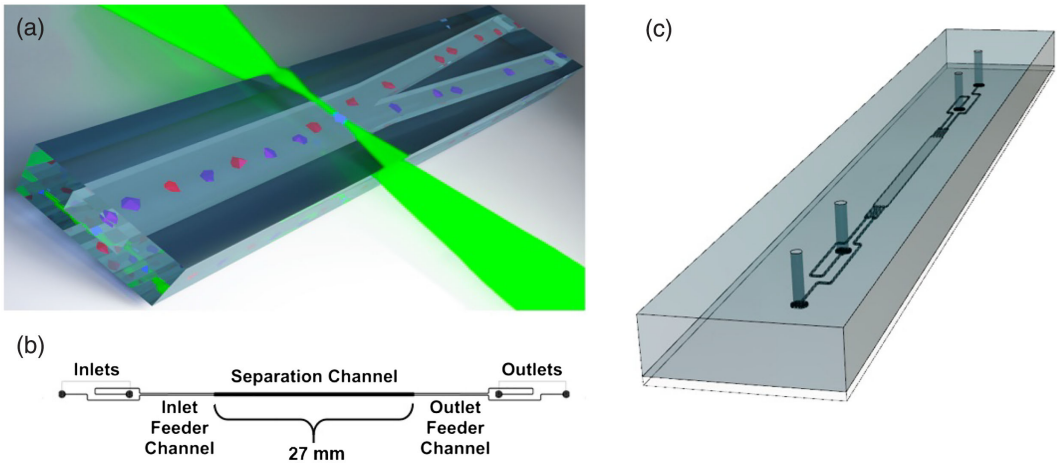

Fig. 1. Design of a generic optofluidic sorting device. (a) Artistic view of the microfluidic device while passively sorting particles using an orthogonal laser beam. (b) 2D layout of the actual optofluidic device. (c) Perspective view of a completed sorting device, not to scale.

outlet ports, and a 27-mm-long separation chamber. Devices are cut or diced to 5-mm-wide strips; a narrow device allows easier optical coupling. Optical faces were created on the outer sides by varying methods depending on the device type. Separation is viewed from the top or bottom, and the optical force beam is focused inside the channel through the sides. We pursued three methods of fabrication: (1) molded polydimethylsiloxane (PDMS), (2) laser etched Borofloat33 (BF33), and (3) DRIE fused silica.

A. PDMS Device Fabrication

100-μm features were fabricated on a 76.2-mm silicon wafer using SU-8 photolithography. The process was as recommended by the supplier (GM1070, Gersteltech Switzerland). The photomask was a commercial chrome on soda lime mask with the sidewall of the sorting chamber parallel to the mask edge to eliminate staircase patterning.

An SU-8 master mold was used to create PDMS daughter molds using soft lithography (Sylgard 184, Ellesworth Adhesives Australia). Mixed and degassed polymer was poured onto the mold and cured at 65°C for at least 2 h. After the PDMS had set, it was peeled from the master mold and applied to a clean acrylic sheet where fluid ports were punched using a biopsy punch. Individual devices were then cut to size using a blade [Fig. 1(c)]. The molded devices were bonded to 5-mm-wide strips of coverglass. To create smooth external faces for beam coupling, the devices were placed on their side on a glass slide (Sail Brand 7101), and freshly degassed liquid PDMS was then used to fill the gap between the glass and the device. After curing, the process was repeated on the other side and excess PDMS trimmed.

B. Laser Etched Device Fabrication

The surface of a 1-mm-thick BF33 glass substrate was prepared for etching with a protective layer of a few micrometers of AZ 1518 photoresist (MMRC Australia). The channels were laser etched at the Optofab node of the Australian National Fabrication Facility of Macquarie University. The facility used a 532-nm picosecond laser (Lumera SuperRapid-He) to ablate the surface based on a 2D design of the channel. The process uses the nonlinear absorption of atoms at the laser focus to generate a strong electric field. This electric field results in the ionization of the atoms, which removes the material as it transitions to plasma [12,13]. The etch rate and depth were determined as a function of laser power (300 mW), scan speed (12.5 mm/s), and number of passes (25) to produce an 80-μm-deep channel. The laser power was then increased to 1 W to drill the 500-μm fluidic ports.

An N-methylpyrrolidinone (NMP) bath was used to remove the AZ1518 photoresist to prepare the surface for bonding. The etched surface was bonded with a 150-μm-thick BFF33 wafer using thermo-compression bonding on an EVG-520 hot embossing machine at the ANFF-South Australia. The lidded devices were then diced into individual 5-mm-wide devices using a wet disc saw. Thin strips of coverglass were optically glued onto the side surfaces using Norland Optical adhesive (NOA81).

C. Deep Reactive Ion Etched Device Fabrication

A 100-mm- fused silica substrate was patterned using a SU-8 photoresist to define the channel. The etching process was completed at ANFF-South Australia using C_3F_8 as the etching gas and a ULVAC NLD570 tool. This process uses the combination of plasma and C_3F_8 to breakdown the substrate in the areas that are not protected with photoresist by ionization [14]. After the channel was etched, the wafers were re-coated in SU-8 resist and office taped to protect the surface during sand-blasting of fluidic ports. These were created using a dental sand-blaster (Danville Materials Microetcher, Zest Dental Solutions California).

To remove the resist and prepare the substrate for bonding, we soaked the wafers in warm NMP. The etched surface of the wafer and a 110-μm wafer were prepared for bonding with a piranha clean and ammonia hydroxide bath. The two surfaces were dried and pressed together on a flat surface to form a temporary bond. These bonded pieces were then annealed in an oven at 1000°C for 24 h. The lidded piece was returned to ANFF-South

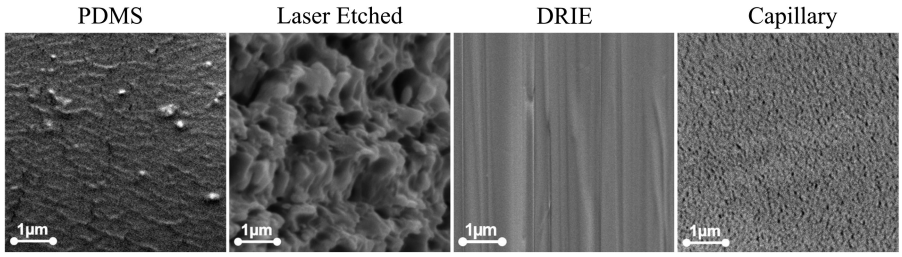

Fig. 2. Sidewall images created by scanning electron microscope.

Australia for wet disc saw dicing. Thin strips of coverglass were optically glued onto the side surfaces using NOA81.

3. SIDEWALL SURFACE CHARACTERIZATION

Efficient coupling of light into the microfluidic chamber is important for maintaining laser power and forward momentum. The external surfaces of the various devices were made optically flat as described earlier, but the roughness of the sidewall of the microfluidic chamber varies with fabrication method. To gain an indication of the surface roughness of the sidewalls, we used scanning electron microscopy (SEM) to image the interior walls of each channel (see Fig. 2). The inner surface of a drawn rectangular glass capillary (CM Scientific, United Kingdom) is included as a reference.

On the PDMS devices, small cracks occurred due to the sheering removal of the peel, and small impurities likely adhered to the surface during handling and preparation for SEM. The average feature in the PDMS image was on the order of 200 nm. The sidewall of the laser etched channel featured a carpet-like texture that was uniformly covered by 500-nm-sized lumps. The DRIE sidewall varied with position on the wafer. Near the perimeter, there were significant grass-like artifacts that extended down the sidewall exceeding 1 μm in roughness. However, the sidewall in the channel, (away from the wafer perimeter) was very smooth (Fig. 2). The sidewall of the capillary was also very smooth, and we suspect the roughness in the picture is largely caused by the gold coating.

4. OPTICAL TRANSMISSION

Optofluidic sorting uses radiation pressure, also known as the scattering force, given by

$$F_{\text{scatt}} = \frac{n_m}{c}\sigma I, \tag{1}$$

where $\sigma = \frac{8}{3}\pi k^4 r^6 (\frac{m^2-1}{m^2+2})^2$ is the scattering cross section of the particle [15], I the intensity of the laser beam, r the radius of the particle, k the wave vector, and m the ratio of refractive indices $\frac{n_p}{n_m}$, where n_p is the refractive index of the particle, and n_m is the refractive index of the medium. The particles are subjected to the viscosity of the fluid. For a sphere of radius r, the drag force is given by Stokes' law [16]:

$$F_{\text{Stokes}} = 6\pi\eta r v, \tag{2}$$

where η is the dynamic viscosity of the medium, and v is the particle velocity. This optical force is along the direction of propagation and proportional to the light intensity. It is therefore critical to transmit as much beam power as possible into the fluid channel with minimal diffuse scattering.

We have characterized the optical properties of these devices by looking at optical transmission. We expected the transmitted laser power to decrease due to scattering within the medium (attenuation) and at the interfaces between different media (refraction and reflection). For this experiment, we varied the channel conditions from wet to dry and characterized the transmission for two laser colors: 532 nm and 700 nm. We configured the optical path to be a focused beam inside the microfluidic channel with a waist of ≈ 3 μm and Rayleigh length of ≈ 35 μm for both colors. We took particular care that the waist of the beam inside the devices was always smaller than the channel height. The power was measured using a Thorlabs optical power meter placed 180 mm from the device. The power meter used a S120C standard photodiode power sensor with a detection diameter of 9.5 mm to measure the power. Transmission is defined as the laser power received with the device in place divided by the power received with the device removed from the optical path. Measurements were recorded at five points along the length of the separation channel before the device was flipped (to reverse the path), and the experiment was repeated. The results were averaged and are shown in Fig. 3.

As expected, we see that wetting the channel improved the optical transmission under all test conditions, as the higher refractive index of water reduces the losses due to refraction at the interior interface. Despite exhibiting very low roughness, the PDMS device performed poorly. It is possible that light was lost due to refraction at the glass–PDMS interface. The index of PDMS is ~1.4, slightly less than glass. If the fabrication of the device were modified so that the molded device was bonded to a thick slab of PDMS, we hypothesize that optical transmission would improve.

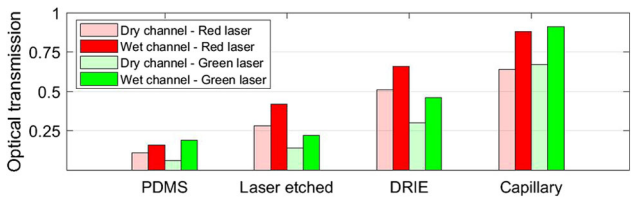

Fig. 3. Optical transmission of each microfluidic chip. Transmission is measured for a wet and dry channel with a green (532 nm) and red (700 nm) laser.

The coarse finish of the laser etched sidewall prevented both of the laser colors from effectively crossing the channel. The DRIE device exhibited effective coupling for all of the test conditions, and the square capillaries exhibited the best optical coupling.

5. SCATTERING EXPERIMENT

In the following, we selected the best fabricated device (etched fused silica) and compared its performance with a commercially available capillary. In particular, we were interested in the difference of radiation pressure force between the two devices. The square capillary had an outer dimension of 400 μm and an inner side length of 200 μm. We filled the channel with a solution of fluorescent polystyrene particles (PolySciences Fluoresbrite YG Microspheres) of average diameter 0.5 μm to observe the optical scattering force. The channel is imaged from the top using a microscope objective (NA = 0.6). We characterize the interaction between the suspended particles and the laser that crosses the channel perpendicular to the observation path (see Fig. 1). We recorded videos to track the motion of the particles and to quantify the optical forces acting on them. In order to analyze the videos, we fed them to a Lagrangian particle tracking algorithm (described in Ref. [17]), which allowed us to quantify the effect of the laser on the particles. For the data presented in Figs. 4 and 5, we worked with a laser power fixed at 200 mW at 532 nm.

In Fig. 4(a), we plot the amplitude of the instantaneous velocity vector in the DRIE device. The pushing effect of the laser can be seen in the white rectangle; the particles are pushed to the right by the laser. Figures 4(b) and 4(c) show the horizontal and vertical velocities in the channel for each vertical position by averaging over the horizontal axis. We can retrieve the width of the laser beam inside the channel. Approximating to a Gaussian

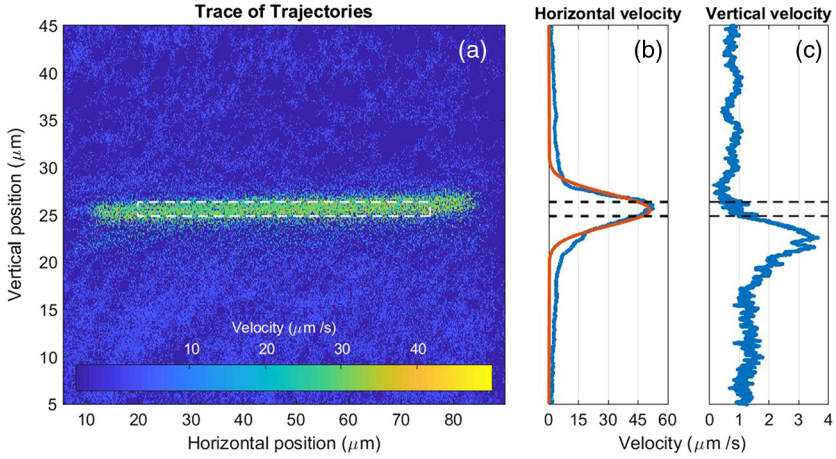

Fig. 4. (a) Example plot of the amplitude of the velocity vector of each particle tracked over 4000 frames. Particles interacting with the laser are accelerated, resulting in a large velocity. The region of high velocities in the center of the channel indicates the position of the laser beam. (b), (c) Horizontal and vertical velocity averaged over the horizontal direction. The red curve in (b) is a Gaussian fit.

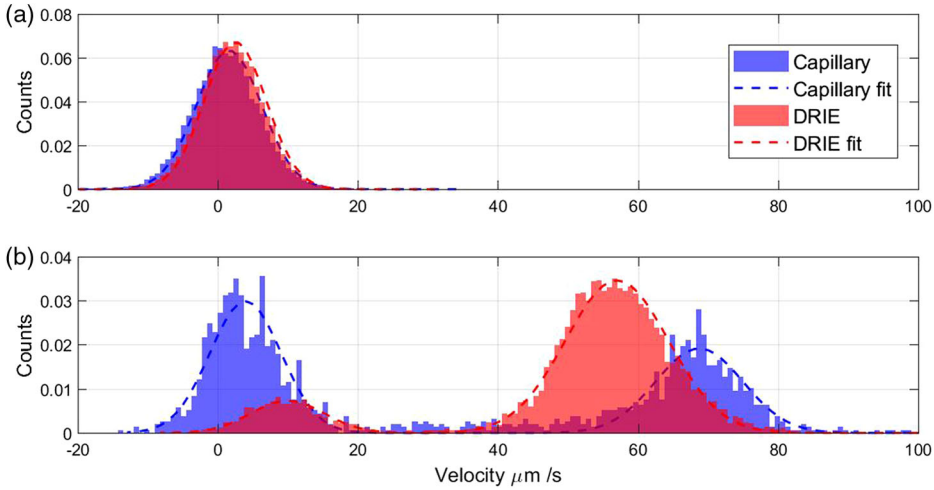

Fig. 5. Comparison of the particles' behavior in the DRIE device (4440 tracked events) against particles in the glass capillary (2416 tracked events). Each plot shows the horizontal velocity distribution of the particles parallel to the beam axis, normalized for probability. (a) Gaussian velocity distributions of the particles outside of the beam axis typical of Brownian motion. (b) Velocity distributions of the particles inside the beam. In this case, there is a bimodal distribution for both devices, indicative of particles that are pushed by the device (high velocity) and those that are not (low velocity).

beam [see red curve in Fig. 4(b)], we infer a waist of ∼2 μm, in agreement with our optical configuration. Further processing of these trajectories used the pixel location and the displacement of the particles between frames to calculate velocity.

In these data, the vertical flow of the sample was +1 μm/s (upwards). We observe a peak in the vertical velocity due to dipole or gradient force (i.e., an optical tweezing effect) as particles are pulled into the beam. It is worth noting that this effect can be very useful for a sorting device: it effectively increases the active part of the device by drawing particles from lower intensity regions to the focus, where the force is larger and more consistent.

From the 2D map of velocity amplitude [Fig. 4(a)], we define two zones: inside the beam [delimited by the white dashed rectangle in Fig. 4(a)] and outside the beam, defined as everything above 30 μm and below 20 μm. We then calculate the horizontal (in the direction of the beam) velocity distribution inside and outside. We perform this analysis for both the DRIE fabricated microfluidic device and glass capillary. The results are compared in Fig. 5.

Outside the beam [Fig. 5(a)], the velocity distribution is a Gaussian distribution approximately centered around zero. The distribution is due to the Brownian motion of the particle in the viscous fluid. The width of the distribution depends on the temperature of the medium and the size of the particles as well as the dynamic viscosity, which does not change between our devices. Indeed, we expect that for higher (lower) temperature, the width will be broader (narrower), and that for smaller (bigger) particles, the distribution will be narrower (broader). It is interesting to note that the frame rate used to observe the motion will also influence the distribution width. This distribution will be narrower for faster frame rates, since the particles do not have sufficient time to disperse, consistent with Brownian motion.

Looking now at the behavior of the particles inside the beam [see Fig. 5(b)], we observe a bimodal distribution for both the capillary and DRIE device. The distribution of particles with a large velocity is the particles that are pushed by the incident laser. The distribution centered near zero is attributed to tracked particles that are imaged but are not at the same depth as the laser beam and therefore do not get pushed by the beam. The microfluidic channel is much deeper than the objective focal depth, which is larger still than the beam waist. The measured velocities are spread out as a normal distribution; we use its center to extract the velocity v_{in} inside the beam.

Velocity distributions for particles inside the beam are bimodal. They comprise a group of particles that are strongly pushed by the beam and a group that has almost no net velocity. These groups are fitted to single Gaussians (dashes lines). Inside the DRIE device, the particles are pushed with a mean velocity of $v_{in}^{\mathrm{DRIE}} = 56.2 \pm 7.5$ μm/s. Inside the capillary device, the particles are pushed with a mean velocity of $v_{in}^{\mathrm{capi}} = 66.5 \pm 7.6$ μm/s.

The distributions close to zero are not centered at exactly zero, and it is larger for the DRIE device $v_{\mathrm{drag}}^{\mathrm{DRIE}} = 9.7$ μm/s than for the capillary $v_{\mathrm{drag}}^{\mathrm{capi}} = 3.4$ μm/s. We attribute this non-zero velocity to a drag force caused by flow in the fluid arising from a significant number of particles being pushed. In each case, the particle density is constant; however, the devices have different internal dimensions. The DRIE device is 500 μm in the direction of the beam, while the capillary is 200 μm. We suggest that this additional length leads to higher fluid drift velocity in the beam direction.

The mean velocity for the two populations (DRIE and capillary) was used to calculate the strength of the optical scattering force (F_{scatt}) [Eq. (1)], where $n_p = 1.59$ (polystyrene), $n_m = 1.33$ (water), and $\eta = 0.89$ mPa.s (water at 25°C); v is the particle velocity. We assume that the particles are reaching their terminal velocity as soon as they are captured by the beam, as we do not see a variation in velocity along its propagation axis. We estimate the radiation pressure force applied by the laser on the particles as 236 fN in the DRIE and 279 fN in the capillary. The difference is consistent with the difference in laser power transmission.

6. CONCLUSION

An optofluidic device for radiation pressure particle sorting was created using three different fabrication methods. The sidewall surfaces of these devices were physically and optically characterized and compared with a drawn glass capillary of rectangular cross section. The DRIE etched device had better optical transmission than both a laser etched device and a PDMS device fabricated by SU-8 and soft lithography. The optical forces exerted on 0.5-μm polystyrene particles in the DRIE device and the glass capillary were measured. The optical force inside the DRIE device was 15% lower than in the glass capillary, which is consistent with the difference in optical transmission.

Funding. Australian Research Council (DP170103010).

Acknowledgment. Part of this work was performed at the South Australian and OptoFab nodes of the Australian National Fabrication Facility under the National Collaborative Research Infrastructure Strategy.

Disclosures. At the time of submission, James White is employed by Engender Technologies (Hamilton New Zealand). Engender Technologies is developing optofluidic devices for biotechnology (Commercial Relationships Disclosure Code E). All other authors declare no conflicts of interest.

REFERENCES

1. A. Ashkin, "Acceleration and trapping of particles by radiation pressure," Phys. Rev. Lett. **24**, 156–159 (1970).
2. D. S. Bradshaw and D. L. Andrews, "Manipulating particles with light: radiation and gradient forces," Eur. J. Phys. **38**, 034008 (2017).
3. T. Yang, P. Paiè, G. Nava, F. Bragheri, R. Martinez Vazquez, P. Minzioni, M. Veglione, M. D. Tano, C. Mondello, R. Osellame, and I. Cristiani, "An integrated optofluidic device for single-cell sorting driven by mechanical properties," Lab Chip **15**, 1262–1266 (2015).
4. F. Bragheri, P. Minzioni, R. M. Vazquez, N. Bellini, P. Paiè, C. Mondello, R. Ramponi, I. Cristiani, and R. Osellame, "Optofluidic integrated cell sorter fabricated by femtosecond lasers," Lab Chip **12**, 3779–3784 (2012).
5. W. Wu, X. Zhu, Y. Zuo, L. Liang, S. Zhang, X. Zhang, and Y. Yang, "Precise sorting of gold nanoparticles in a flowing system," ACS Photon. **3**, 2497–2504 (2016).

6. K. D. Leake, B. S. Phillips, T. D. Yuzvinsky, A. R. Hawkins, and H. Schmidt, "Optical particle sorting on an optofluidic chip," Opt. Express **21**, 32605–32610 (2013).
7. G. Tkachenko and E. Brasselet, "Optofluidic sorting of material chirality by chiral light," Nat. Commun. **5**, 3577 (2014).
8. E. Hecht, *Optics*, 4th ed. (Addison-Wesley, 2002).
9. K. Sugioka and Y. Cheng, "Femtosecond laser processing for optofluidic fabrication," Lab Chip **12**, 3576–3589 (2012).
10. S. Thiele, K. Arzenbacher, T. Gissibl, S. Schmidt, H. Gross, H. Giessen, and A. Herkommer, "Design, simulation and 3D printing of complex micro-optics for imaging," in *International Conference on Optical MEMS and Nanophotonics (OMN)* (2016), pp. 1–2.
11. A. R. Hawkins and H. Schmidt, "Optofluidic waveguides: II. Fabrication and structures," Microfluid. Nanofluid. **4**, 17–32 (2008).
12. D. Nieto, J. Arines, G. M. O'Connor, and M. T. Flores-Arias, "Single-pulse laser ablation threshold of borosilicate, fused silica, sapphire, and soda-lime glass for pulse widths of 500 fs, 10 ps, 20 ns," Appl. Opt. **54**, 8596–8601 (2015).
13. P. G. Eliseev, O. N. Krokhin, and I. N. Zavestovskaya, "Nonlinear absorption mechanism in ablation of transparent materials by high power and ultrashort laser pulses," Appl. Surf. Sci. **248**, 313–315 (2005).
14. H. Jansen, H. Gardeniers, M. de Boer, M. Elwenspoek, and J. Fluitman, "A survey on the reactive ion etching of silicon in microtechnology," J. Micromech. Microeng. **6**, 14–28 (1996).
15. M. Kerker, *Scattering of Light and Other Electromagnetic Radiation* (Elsevier, 2016).
16. G. K. Batchelor, *An Introduction to Fluid Dynamics* (Cambridge University, 1967).
17. N. T. Ouellette, H. Xu, and E. Bodenschatz, "A quantitative study of three-dimensional Lagrangian particle tracking algorithms," Exp. Fluids **40**, 301–313 (2006).